

# Valence-bond solid to antiferromagnet transition in the two-dimensional Su-Schrieffer-Heeger model by Langevin dynamics

A. Götz,<sup>1</sup> S. Beyl,<sup>1</sup> M. Hohenadler,<sup>1</sup> and F. F. Assaad<sup>1,2</sup>

<sup>1</sup>*Institut für Theoretische Physik und Astrophysik, Universität Würzburg, 97074 Würzburg, Germany*

<sup>2</sup>*Würzburg-Dresden Cluster of Excellence et.qmat, Am Hubland, 97074 Würzburg, Germany*

The two-dimensional Su-Schrieffer-Heeger model of electrons coupled to quantum phonons is investigated using Langevin dynamics within the framework of auxiliary-field quantum Monte Carlo. Based on an explicit determination of the density of zeros of the fermion determinant, it is argued that the method is efficient in the challenging adiabatic limit. Large-scale simulations at the  $O(4)$ -symmetric point establish that the ground state of the 2D SSH model undergoes a transition from a  $(\pi, \pi)$  valence bond solid to an antiferromagnet with increasing phonon frequency, yet still in the adiabatic regime. The single-particle spectrum illustrates the renormalization of the electronic band and suggests the existence of a gapped polaronic band, whereas the particle-hole channels show gapless modes associated with long-range bond and magnetic order, respectively. The simulations are supplemented with a mean-field analysis and a self-consistent Born approximation.

## I. INTRODUCTION

The coupling of electrons or spins to phonons can generate many fascinating states of matter. Apart from superconductivity [1], this also includes phases that break lattice symmetries such as charge-density wave states (CDW) and various flavors of valence-bond solid (VBS) states [2]. In spin systems, the coupling to phonons can generate quantum phase transitions between antiferromagnetic (AFM) and VBS states [3]. A particularly intriguing aspect is the possibility of realizing quantum phase transitions beyond the Landau-Ginzburg-Wilson paradigm—connecting two states with different local order parameters—in models relevant for materials.

The Debye frequency  $\omega_D$  is typically much smaller than the Fermi energy  $\epsilon_F$ . This separation of energy scales underlies Migdal’s theorem [1, 4], which provides a small parameter,  $\hbar\omega_D/\epsilon_F$ , to justify perturbative approaches to the electron-phonon problem. Quantum Monte Carlo (QMC) simulations offer the possibility to take a step beyond perturbative approaches and thereby investigate competing instabilities [5]. In fact, the generic electron-phonon problem does not suffer from a negative sign problem, irrespective of lattice geometry and band filling. In particular, for each space-time configuration of phonon fields, time-reversal symmetry ensures that the eigenvalues of the fermion determinant come in complex conjugate pairs [6]. As such, it should be a technically simple problem. However, this is not the case. First, the argument for the absence of a negative sign problem is valid only if the phonons are not integrated out, as done in Refs. [7–9]. For example, the continuous-time interaction expansion (CT-INT) QMC method [7] suffers, in general, from a negative sign problem when applied to two-dimensional (2D) electron-phonon problems. The approach introduced in Ref. [9] for the Hubbard-Holstein model is free of a sign problem but only part of the parameter space is accessible. Even in the absence of a sign problem, a central challenge is to find an adequate sampling scheme that deals with the separation of en-

ergy scales. Adopting a local updating scheme—as commonly used in QMC simulations of fermions—in which the phonon field is updated on a time scale set by the electron motion, leads to prohibitively long autocorrelation times [10]. Global updates of the phonon fields on the imaginary time scale of the inverse Debye temperature are highly desirable and have been achieved using, for example, self-learning methods [11]. Finally, a sufficiently favorable scaling of the numerical effort with system size is essential to study phase transitions.

The history of unbiased numerical results for 2D systems of electrons coupled to quantum phonons directly reflects these algorithmic challenges. QMC investigations focused on the two fundamental types of interactions captured by the Holstein [12] and Su-Schrieffer-Heeger (SSH) Hamiltonians [13], respectively. Simulations of Holstein-type models have a long history, mainly in connection with CDW formation and superconductivity (SC), but many important questions have only been resolved recently, see, e.g., Ref. [14] and references therein. QMC simulations of the simplest variant of the SSH model, namely a half-filled square lattice, have remained elusive until recently when the long-standing discussion regarding the pattern of the expected VBS ground state was resolved in Ref. [15].

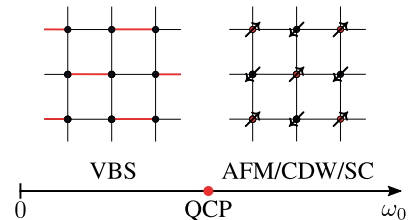


FIG. 1. Schematic phase diagram of the  $O(4)$ -symmetric, square-lattice SSH model as a function of phonon frequency. The left inset depicts the VBS phase, showing one of four equivalent  $(\pi, \pi)$  patterns of strong and weak bonds. The right inset illustrates the AFM phase which, due to the  $O(4)$  symmetry, is equivalent to a phase with CDW or SC order.

Here, we investigate the 2D SSH model with optical phonons on the square lattice and for the case of a half-filled band. We focus on the high-symmetry point with partial particle-hole symmetry that exhibits an  $O(2N)$  symmetry for the general case of fermions with  $N$  flavors.

The purpose of our work is twofold. First, we investigate the usefulness of Langevin updates, successfully applied before to the 2D Holstein model [16], by using an identical algorithm based on the standard auxiliary-field QMC (AFQMC) formulation [17] implemented in the ALF-2.0 package [18]. Our analysis is based on the calculation of a Pfaffian whose sign changes track the zeros of the fermion determinant. Following Ref. [16], we also implemented Fourier acceleration to reduce autocorrelations. Our analysis reveals that the method is suited to investigate the particularly interesting adiabatic regime.

Second, we provide insight into the physics of the SSH model, namely evidence for and details of a transition from a VBS state to an AFM state with increasing phonon frequency. A schematic phase diagram is shown in Fig. 1. AFM order at finite phonon frequencies is remarkable as it was expected only in the presence of Coulomb repulsion [19–23]. We characterize the evolution with phonon frequency by calculating susceptibilities and, in particular, excitation spectra. We complement our numerical results with those from a self-consistent Born approximation. Furthermore, we determine the mean-field ground state and study its destruction by thermal fluctuations in the adiabatic limit.

The rest of the article is organized as follows. In Sec. II, we define the SSH model and comment on symmetries, limiting cases, and previous work. In Sec. III, we discuss the numerical method. Our results are presented in Sec. IV, followed by a discussion in Sec. V. We also provide an appendix with details about the self-consistent Born approximation.

Aspects of this work were already reported in Ref. [24].

## II. MODEL AND SYMMETRIES

### A. Hamiltonian

We consider an SSH model with optical phonons, defined by the Hamiltonian

$$\begin{aligned} \hat{H}_{\text{el}} = & -t \sum_{\langle i,j \rangle} \sum_{\sigma=1}^N \left( \hat{c}_{i,\sigma}^\dagger \hat{c}_{j,\sigma} + \text{h.c.} \right) + \sum_b \left[ \frac{\hat{P}_b^2}{2m} + \frac{k}{2} \hat{Q}_b^2 \right] \\ & + g \sum_{\langle i,j \rangle} \hat{Q}_b \sum_{\sigma=1}^N \left( \hat{c}_{i,\sigma}^\dagger \hat{c}_{j,\sigma} + \text{h.c.} \right). \end{aligned} \quad (1)$$

The first term describes the hopping of electrons on the bonds  $b = \langle i, j \rangle$  connecting two nearest-neighbor sites  $i$ ,  $j$  with hopping amplitude  $t$ . The operator  $\hat{c}_{i,\sigma}^\dagger$  creates an electron in a Wannier state centered at site  $i$  and with

$z$ -component of spin  $\sigma$  that runs over  $N$  flavors. We use anti-periodic boundary conditions  $\hat{c}_{i+L\mathbf{a}_1,\sigma}^\dagger = -\hat{c}_{i,\sigma}^\dagger$  in the direction of the primitive vector  $\mathbf{a}_1$  of the lattice and periodic boundary conditions  $\hat{c}_{i+L\mathbf{a}_2,\sigma}^\dagger = \hat{c}_{i,\sigma}^\dagger$  in the direction of  $\mathbf{a}_2$ . The phonons are represented by harmonic oscillators that reside on the bonds. They are described by momentum and position operators  $\hat{P}_b$  and  $\hat{Q}_b$  as well as the frequency  $\omega_0^2 = k/m$ , where  $k$  is the spring constant and  $m$  the mass of the harmonic oscillators. Electron hopping is modulated by the coupling to the phonon coordinate  $\hat{Q}_b$  on the respective bond  $b$  with strength  $g$ . The adiabatic regime is defined as  $\omega_0 < t$ . All results will be for  $N = 2$  (i.e., spin-1/2 electrons).

### B. Symmetries

The SSH model at half-filling and on a bipartite lattice is invariant under the partial particle-hole transformation

$$\hat{P}_\sigma^{-1} \hat{c}_{i,\sigma}^\dagger \hat{P}_\sigma = \delta_{\sigma,\sigma'} e^{i\mathbf{Q} \cdot \mathbf{i}} \hat{c}_{i,\sigma'} + (1 - \delta_{\sigma,\sigma'}) \hat{c}_{i,\sigma}^\dagger \quad (2)$$

where  $\mathbf{Q} = (\pi, \pi)$  for the square lattice considered here. We can define a corresponding  $\mathbb{Z}_2$  order parameter, the fermion parity on site  $i$  [25],

$$\hat{p}_i = \prod_{\sigma=1}^N (1 - 2\hat{n}_{i,\sigma}). \quad (3)$$

This Ising-like order parameter supports order at finite temperature. Since it changes sign under transformation (2), it can be used to detect a spontaneous breaking of the particle-hole symmetry.

In addition to the apparent global  $SU(N)$  spin rotation symmetry, the model possesses an enlarged  $O(2N)$  symmetry on a bipartite lattice. To prove this, we reformulate the Hamiltonian using Majorana fermions [25, 26]

$$\hat{c}_{i,\sigma}^\dagger = \frac{1}{2} (\hat{\gamma}_{i,\sigma,1} - i\hat{\gamma}_{i,\sigma,2}). \quad (4)$$

After a canonical transformation  $\hat{c}_i^\dagger \rightarrow i\hat{c}_i^\dagger$  on one sublattice, the hopping operator can be written as

$$\hat{K}_b = \sum_{\sigma=1}^N \left( \hat{c}_{i,\sigma}^\dagger \hat{c}_{j,\sigma} + \text{h.c.} \right) = \frac{i}{2} \sum_{\sigma} \sum_{\alpha=1}^2 \hat{\gamma}_{i,\sigma,\alpha} \hat{\gamma}_{j,\sigma,\alpha}, \quad (5)$$

thereby revealing the  $O(2N)$  symmetry. Because of the latter, the model is free of a sign problem for odd values of  $N$  [27]. For even  $N$ , time-reversal symmetry is sufficient to show the absence of a sign problem [6]. In the case of  $N = 2$  considered here, the spin operators and the Anderson pseudospin operators [28] are the infinitesimal generators of the  $SO(4)$  symmetry. They are defined by

$$\hat{\mathbf{S}}_i = \frac{1}{2} \sum_{\sigma,\sigma'} \hat{c}_{i,\sigma}^\dagger \boldsymbol{\sigma}_{\sigma,\sigma'} \hat{c}_{i,\sigma'}, \quad \hat{\boldsymbol{\eta}}_i = \hat{P}_i^{-1} \hat{\mathbf{S}}_i \hat{P}_i, \quad (6)$$

where the vector  $\boldsymbol{\sigma}$  contains the three Pauli matrices. The spin and pseudospin components  $(l, m, n)$  fulfill the Lie algebra of the  $SU(2)$  group  $[\hat{S}_{i,l}, \hat{S}_{j,m}] =$

$i\delta_{i,j} \sum_n \varepsilon_{lmn} \hat{S}_{i,n}$  and commute among each other. Here,  $\varepsilon_{lmn}$  is the Levi-Civita symbol. The Lie algebra of the global  $O(4)$  symmetry can be interpreted as  $O(4) = SU(2) \times SU(2) \times \mathbb{Z}_2$ , where the additional  $\mathbb{Z}_2$  symmetry corresponds to the partial particle-hole symmetry [25]. Hence, an AFM phase is degenerate with a CDW and an s-wave superconductor (SC). If the parity  $\hat{p}_i$  orders and the particle-hole symmetry is spontaneously broken, either the spin or charge sector is explicitly chosen. The VBS ground state in Fig. 1 spontaneously breaks the  $C_4$  symmetry of the lattice, whereas long-range AFM order breaks the  $O(4)$  symmetry down to  $U(1)$ .

### C. Limiting cases

In the adiabatic limit  $\omega_0 \rightarrow 0$ , imaginary-time fluctuations of the phonon fields are exponentially suppressed. The phonon displacements can be treated classically and the Hamiltonian can be written as

$$\hat{H} = \sum_b (-t + gq_b) \hat{K}_b + \sum_b q_b^2. \quad (7)$$

Here,  $\hat{Q}_b|q\rangle = q_b|q\rangle$  and  $\hat{K}_b$  is defined in Eq. (5). The Hamiltonian consists solely of a modulated hopping of the electrons and the potential energy of the phonon fields. Mean-field theory or Monte Carlo simulations yield a VBS ground state, see Sec. IV A.

For  $\omega_0 > 0$ , we can integrate out the phonons to obtain an effective Hamiltonian for the electrons [25, 29]. This yields the action

$$S_{\text{eff}} = -\frac{g^2}{2k} \int_0^\beta \int_0^\beta d\tau d\tau' \sum_b \hat{K}_b(\tau) D(\tau - \tau') \hat{K}_b(\tau') \quad (8)$$

with  $\beta = T^{-1}$  the inverse temperature (we set  $k_B = 1$ ). The interaction is local but retarded,

$$D(\tau) = \frac{\omega_0}{2} \frac{e^{-\omega_0|\tau|} + e^{-\omega_0(\beta-|\tau|)}}{1 - e^{-\omega_0\beta}}. \quad (9)$$

By taking the antiadiabatic limit  $\omega_0 \rightarrow \infty$ , it becomes instantaneous [25],

$$\lim_{\omega_0 \rightarrow \infty} D(\tau) = \delta(\tau). \quad (10)$$

The effective Hamiltonian of the SSH model in the antiadiabatic limit is given by

$$\hat{H}_{\text{eff}} = -t \sum_{\langle i,j \rangle} \hat{K}_b - \frac{g^2}{2k} \sum_{\langle i,j \rangle} \hat{K}_b^2. \quad (11)$$

For  $N = 1$ , this expression is equivalent to the Hamiltonian of the  $t$ - $V$  model if we set  $g = \sqrt{kV}$ . For two fermion flavors,  $N = 2$ , we can rewrite the interaction term as

$$-\frac{1}{4} \hat{K}_b^2 = \hat{S}_i \cdot \hat{S}_j + \hat{\eta}_i \cdot \hat{\eta}_j. \quad (12)$$

The interaction (12) again reveals the  $O(4)$  symmetry and favors an AFM/CDW/SC ground state [25].

### D. Previous work

Despite its long history [13], the SSH model was mainly studied in connection with 1D materials. Until recently, investigations of the 2D SSH model relied on mean-field arguments or started outright from the adiabatic limit of classical phonons. The correct mean-field VBS pattern remained controversial [19, 30–32] and an alternative, multi-mode Peierls state with no well-defined ordering wavevector was suggested [33–35]. AFM order in 2D SSH models with additional Coulomb interaction was discussed in Refs. [19–23]. However, all these works completely left out the impact of quantum lattice fluctuations, which are the focus of the present work and have proven to have a crucial impact for the 1D spinless (i.e.,  $N = 1$ ) SSH model [36]. Numerical confirmation of the existence of a unique VBS ground state and its ordering pattern was provided by QMC simulations in Ref. [15], where a nonzero critical value was reported for quantum phonons. QMC results were also obtained for the honeycomb lattice [37] and the Lieb lattice [38].

## III. METHODS

### A. Langevin dynamics

Using the real-space formulation of the path integral for the phonon degrees of freedom with the eigenstates  $|q\rangle$  of the position operator  $\hat{Q}_b$ , the partition function of the model can be written as

$$Z = \int \prod_{b,\tau} dq_{b,\tau} e^{-S}, \quad (13)$$

$$S = S_0 + S_F = S_0 - N \ln \det [\mathbf{1} + B(\beta, 0)]$$

with

$$B(\tau_1, \tau_2) = \prod_{\tau=\tau_2+\Delta\tau}^{\tau_1} \left( \prod_b e^{-\Delta\tau g q_{b,\tau} K_b} \right) e^{\Delta\tau t \sum_b K_b} \quad (14)$$

and the matrix

$$(K_b)_{x,y} = \begin{cases} 1 & \text{if } x \in b \wedge y \in b \\ 0 & \text{otherwise} \end{cases}. \quad (15)$$

Here,  $x$  and  $y$  label lattice sites;  $x \in b$  means that site  $x$  belongs to bond  $b$ . In the path integral, we discretized the imaginary time interval  $[0, \beta[$  into steps of width  $\Delta\tau = \beta/L_{\text{Tot}}$ . Following Blankenbecler, Scalapino, and Sugar (BSS) [17] we rewrote the fermionic trace as a determinant. Therefore, we only have to sample the phonon degrees of freedom, whose  $g = 0$  imaginary-time dynamics is governed by

$$S_0 = \Delta\tau \sum_{b,\tau} \left( \frac{1}{\omega_0^2} \left[ \frac{q_{b,\tau+1} - q_{b,\tau}}{\Delta\tau} \right]^2 + q_{b,\tau}^2 \right). \quad (16)$$

We use Langevin dynamics to update the phonon fields  $\mathbf{q} = \{q_{b,\tau}\}$ . The corresponding Langevin equation is a stochastic differential equation for the fields [16, 18],

$$\frac{d\mathbf{q}(t_l)}{dt_l} = -M \frac{\partial S(\mathbf{q}(t_l))}{\partial \mathbf{q}(t_l)} + \sqrt{2M} \boldsymbol{\eta}(t_l), \quad (17)$$

with an additional Langevin time  $t_l$ . The independent Gaussian random variables  $\boldsymbol{\eta}$  satisfy

$$\langle \eta_{b,\tau}(t_l) \rangle = 0, \quad \langle \eta_{b,\tau}(t_l) \eta_{b',\tau'}(t'_l) \rangle = \delta_{b,b'} \delta_{\tau,\tau'} \delta(t_l - t'_l), \quad (18)$$

where  $\delta$  is to be understood as a Kronecker  $\delta$  for the discrete indices and as the Dirac  $\delta$  function for the continuous  $t_l$ . The matrix  $M$  is an arbitrary positive-definite matrix. In order to use the Langevin equation in our AFQMC code, we discretize the Langevin time  $t_l$  with a finite time step  $\delta t_l$ . Using the Euler method, the discretized equation is given by [39]

$$\mathbf{q}(t_l + \delta t_l) = \mathbf{q}(t_l) - M \frac{\partial S(\mathbf{q}(t_l))}{\partial \mathbf{q}(t_l)} \delta t_l + \sqrt{2\delta t_l M} \boldsymbol{\eta}(t_l). \quad (19)$$

For the random variables  $\boldsymbol{\eta}$  we replace  $\delta(t_l - t'_l) \rightarrow \delta_{t_l, t'_l}$ . The systematic error introduced by discretizing  $t_l$  is of linear order in  $\delta t_l$  [16, 18]. By transforming the Langevin equation into a Fokker-Planck equation one can show that the stationary probability distribution of finding the system in state  $\mathbf{q}$  is given by [40]

$$P(\mathbf{q}) = \frac{e^{-S(\mathbf{q})}}{\int D\mathbf{q} e^{-S(\mathbf{q})}}. \quad (20)$$

A major aspect of Langevin dynamics are the forces, their computation, and characteristics. For the SSH model, using Eq. (13), the forces read

$$\frac{\partial S}{\partial q_{b,\tau}} = \Delta\tau k q_{b,\tau} + \frac{m}{\Delta\tau} (2q_{b,\tau} - q_{b,\tau+1} - q_{b,\tau-1}) + N g \Delta\tau \text{Tr} \{K_b (1 - G(b, \tau))\} \quad (21)$$

with the Green function

$$G_{i,j}(b, \tau) = \frac{\text{Tr} \left[ \hat{U}^<(b, \tau) \hat{c}_i \hat{c}_j^\dagger \hat{U}^>(b, \tau) \right]}{\text{Tr} \left[ \hat{U}(\beta, 0) \right]} \quad (22)$$

and the propagators

$$\hat{U}^<(b', \tau) = \hat{U}(\beta, \tau) \prod_{b=b'}^{N_b} e^{-\Delta\tau g q_{b,\tau} \hat{c}_b \hat{c}_b^\dagger K_b \hat{c}_b}, \quad (23)$$

$$\hat{U}^>(b', \tau) = \prod_{b=1}^{b'-1} e^{-\Delta\tau g q_{b,\tau} \hat{c}_b^\dagger K_b \hat{c}_b} e^{\Delta\tau t \sum_b \hat{c}_b^\dagger K_b \hat{c}_b} \hat{U}(\tau - \Delta\tau, 0).$$

Here,  $N_b$  is the total number of bonds on the lattice. From Eq. (13) we see that the action has logarithmic divergences if the determinant vanishes. The  $O(2N)$  symmetry of the model only guarantees that the determinant is non-negative. An advantage of Langevin dynamics is that it amounts to global updates. In each

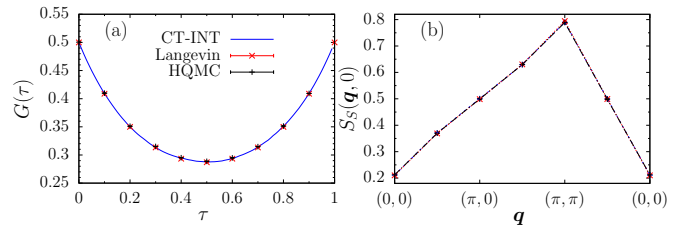


FIG. 2. Comparison of Langevin, CT-INT and HQMC results for (a) the local, imaginary-time Green function and (b) the spin correlation function on an  $L = 4$  lattice for  $\beta = 1.0$ ,  $\Delta\tau = 0.1$ ,  $g = 1.0$ ,  $k = 2$ ,  $\omega_0 = 1.0$ , and  $\delta t_l = 0.0005$ . HQMC and CT-INT data taken from Ref. [26].

step, all phonon fields are updated and, contrary to the Metropolis-Hastings algorithm [41, 42], there is no acceptance-rejection step.

To control the motion through configuration space we used an adaptive Langevin time step  $\delta t_l$  [43, 44]. At each Langevin time step, the fermionic forces for every  $b$  and  $\tau$  are compared to a preset maximal force  $F_{\max}$ . If the maximal computed force  $\max(\partial S_F / \partial q_{b,\tau})$  exceeds  $F_{\max}$ ,  $\delta t_l$  is decreased by the ratio of the two forces,

$$\bar{\delta t}_l = \frac{F_{\max}}{\max \left( \frac{\partial S_F}{\partial q_{b,\tau}} \right)} \delta t_l. \quad (24)$$

The variations of the Langevin time step have to be accounted for when measuring observables,

$$\langle \hat{O} \rangle = \frac{\sum_{\alpha=1}^{N_m} (\bar{\delta t}_l)_\alpha \langle \langle \hat{O} \rangle \rangle_\alpha}{\sum_{\alpha=1}^{N_m} (\bar{\delta t}_l)_\alpha}. \quad (25)$$

Here,  $N_m$  is the total number of measurements and  $\langle \langle \hat{O} \rangle \rangle_\alpha$  denotes the value of the observable  $\hat{O}$  for configuration  $C_\alpha$  of the phonon fields. Equation (25) reduces to  $\langle \hat{O} \rangle = \frac{1}{N_m} \sum_{\alpha=1}^{N_m} \langle \langle \hat{O} \rangle \rangle_\alpha$  for a fixed time step and to  $\langle \hat{O} \rangle = \frac{1}{T_l} \int_0^{T_l} dt_l \langle \langle \hat{O}(t_l) \rangle \rangle$  for continuous Langevin time.

Simulations start from a random field configuration  $\{q_{b,\tau}\}$  and iterate the following set of steps:

1. Compute the equal-time Green functions on all time slices from Eq. (22).
2. Compute the forces via Eq. (21).
3. Using the equal-time Green functions from (1), we can compute  $\langle \langle \hat{O} \rangle \rangle_\alpha$  for any equal-time, multi-point correlation function, see Eq. (25). To this end, we make use of Wick's theorem, which holds for a given field configuration.
4. Adjust the time step according to Eq. (24).
5. Draw a set of independent Gaussian variables  $\boldsymbol{\eta}$ .
6. Compute new fields  $\{q_{b,\tau}\}$  from the Langevin equation using the Fourier acceleration matrix  $M$  and running Langevin time step  $\bar{\delta t}_l$  [Eq. (17)].

In Fig. 2, we compare selected results from our method with two other QMC approaches: the hybrid QMC (HQMC) method described for the SSH model in Ref. [26] and CT-INT QMC method in which the phonons are integrated out in favor of a retarded interaction of the electrons [7, 45, 46]. The results from all three methods are in good agreement.

## B. Calculation of the Pfaffian

In this section, we explore how suitable Langevin dynamics is for the SSH model and in which parameter regions it is particularly efficient or problematic. As opposed to the HQMC approach of Ref. [26], Langevin updates constitute rejection-free global moves. A key requirement for the success of these methods is the *absence* of singularities in the action  $S$ . Since  $S$  contains the logarithm of the fermion determinant, the latter must not vanish. In special cases where  $S$  has no singularities, this class of updating schemes works very well. A notable example is the 1D Hubbard model with open boundary conditions [18]. For the SSH model in the adiabatic limit, the phonon fields are frozen in imaginary time and the fermion determinant is strictly positive. For  $\omega_0 > 0$ , this is not the case.

To analyze the fermion determinant, we derive a relation to a Pfaffian. The latter can be evaluated numerically and its sign changes track the zeros of the determinant. Note that the Pfaffian is not necessary for simulations but rather represents an additional diagnostic.

The  $O(2N)$  symmetry of the model permits us to express the determinant as a square of a trace over one of the two Majorana fermions:

$$Z_\gamma^2 = \det [\mathbf{1} + B(\beta, 0)] \quad (26)$$

$$Z_\gamma = \text{Tr} \left[ \prod_\tau \prod_b \left( e^{-\frac{1}{2} \Delta \tau g q_b, \tau \hat{\gamma}_i \hat{\gamma}_j} \right) e^{\frac{1}{2} \Delta \tau t \sum_b \hat{\gamma}_i \hat{\gamma}_j} \right].$$

Here and in the rest of this section, we drop the spin and Majorana kind indices since none of the quantities considered explicitly depend on them. One can show with a canonical transformation of the Majorana fermions on only one sublattice,  $\hat{\gamma}_i \rightarrow -\hat{\gamma}_i$ , that  $Z_\gamma$  is real [47] and its square hence non-negative.

$Z_\gamma$  can have a different sign in different regions of the configuration space. Being an entire function, it necessarily has to vanish between these regions. Hence, the average sign of  $Z_\gamma$  serves as an estimate of the number of zeros of the determinant. If the average sign is close to plus or minus unity, we are less likely to cross a boundary between two regions in which  $Z_\gamma$  has different signs. In contrast, a small average sign implies more zeros.

To measure the sign of  $Z_\gamma$  we reformulate it as a Pfaffian. First, we use an alternative Trotter decomposition and rewrite the exponentials as hyperbolic functions by

using  $(\hat{\gamma}_i \hat{\gamma}_j)^2 = -1$  to obtain

$$Z_\gamma = \text{Tr} \left[ \prod_x e^{i y_x \hat{\gamma}_i \hat{\gamma}_j} \right] \quad (27)$$

$$= \prod_x (\cosh y_x) \text{Tr} \left[ \prod_x (1 + i \hat{\gamma}_i \hat{\gamma}_j \tanh y_x) \right].$$

The tuple  $x = (b, \tau)$  combines the bond index and the imaginary time slice into a new index ordered according to its position in the product  $\prod_\tau \prod_b$ . To lighten the notation, we used  $y_x = \frac{1}{2} \Delta \tau (t - g q_x)$ . Next, we introduce Grassmann variables  $\xi_{i/j, \tau}$  [29] on every site and imaginary time slice, where  $i$  and  $j$  are on different sublattices, and use

$$C_\pm \prod_{x=1}^n \sqrt{a(x)} = \int [d\xi] e^{\pm \sum_{x < x'} \sqrt{a(x)a(x')} \xi_{x'} \xi_x},$$

$$C_+ = (-i)^n, \quad C_- = 1 \quad (28)$$

for even  $n$  [48]. Here,  $[d\xi] = d\xi_n \dots d\xi_1$  is a time-ordered product and  $a \in \mathbb{C}$ . Finally,  $Z_\gamma$  can be written as the Pfaffian over an antisymmetric matrix  $A \in \mathbb{C}^{2N_b L_{\text{Tot}} \times 2N_b L_{\text{Tot}}}$  [48],

$$Z_\gamma = \prod_x (\cosh y_x) \text{Tr} (1) \text{Pf}(A),$$

where

$$\text{Pf}(A) = \int [d\xi] e^{-\frac{1}{2} \xi^T A \xi} \quad (29)$$

and

$$-\frac{1}{2} \xi^T A \xi = - \sum_x \xi_{i,x} \xi_{j,x} + \sum_{i, (x < x')} m_{x'x} \xi_{i,x'} \xi_{i,x}$$

$$- \sum_{j, (x < x')} m_{x'x} \xi_{j,x'} \xi_{j,x}. \quad (30)$$

Here,  $m_{x'x} = \sqrt{\tanh(y_x) \tanh(y_{x'})}$  and the vector  $\xi$  contains all Grassmann variables.

For the numerical computation of the Pfaffian we used the software from Ref. [49]. Since the calculation is very expensive, we only considered small lattices and a small number of imaginary time slices. In Fig. 3, we plot the average sign for both the t-V model as a function of the interaction strength  $V$  and the SSH model as a function of the phonon frequency  $\omega_0$ .

The results for the t-V model illustrate a breakdown of Langevin dynamics due to severe divergences of the forces. Upon increasing  $V$ , the average sign of the Pfaffian drops to zero and the measured observables deviated by up to a factor of  $10^6$  from results obtained with a Metropolis-Hastings updating scheme. In the adiabatic limit of the SSH model, the average sign is close to unity and the simulations are stable. Increasing  $\omega_0$  leads to a decrease of the average sign and the updating tends to become unstable. In general, we found it easier to stabilize the simulations with our choice of mixed boundary conditions as opposed to periodic boundary conditions in both directions.

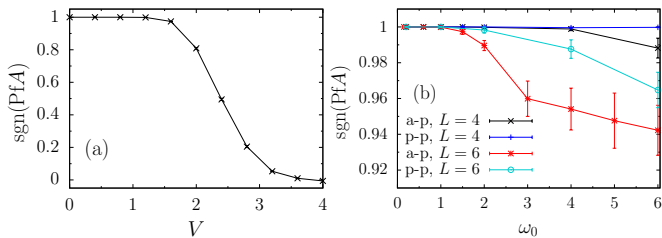


FIG. 3. (a) Average sign of the Pfaffian for the  $t$ - $V$  model on the  $\pi$ -flux square lattice with  $L = 4$ ,  $\beta t = 4$ , and  $\delta t_l = 0.005$ . This model exhibits a Gross-Neveu phase transition at  $V_c = 1.279(3)t$  [50]. (b) Average sign of the Pfaffian for the SSH model with antiperiodic-periodic (a-p) or periodic-periodic (p-p) boundary conditions and  $\beta = 5.0$ ,  $\Delta\tau = 0.1$ , and  $\delta t_l = 0.0005$ .

### C. Fourier acceleration

Following Refs. [16, 40], we used Fourier acceleration to reduce autocorrelations. Its main idea is to increase (reduce) the step size of the Langevin time of slow (fast) phonon modes by using an adequate choice of the matrix  $M$  in the Langevin equation (19) [51].

As a foundation for the choice of  $M$  we consider the non-interacting case ( $g = 0$ ). We carry out a Fourier transformation of the force in imaginary time,

$$\hat{\mathbf{F}} \left[ \frac{dS}{dq_{b,\tau}} \right] = [\Delta\tau k + \frac{2m}{\Delta\tau} (1 - \cos(2\pi\nu_n))] q_{b,\nu_n}. \quad (31)$$

To this end, we defined the Fourier transformation for a function  $f$  as

$$\hat{\mathbf{F}} [f(\tau)] = \frac{1}{L_{\text{Tot}}} \sum_{\tau=1}^{L_{\text{Tot}}} e^{i2\pi\nu_n\tau} f(\tau) \quad (32)$$

with  $\nu_n = \frac{n}{L_{\text{Tot}}}$  with  $n = -\frac{L_{\text{Tot}}}{2} + 1, -\frac{L_{\text{Tot}}}{2} + 2, \dots, \frac{L_{\text{Tot}}}{2}$ . The ratio of the slowest and fastest modes is [16]

$$\frac{(\Delta\tau)^2 k}{(\Delta\tau)^2 k + 4m} \ll 1. \quad (33)$$

Especially for  $\omega_0 \ll 1$ , it is close to zero. We choose the factor  $\tilde{M}(\nu_n)$  in Fourier space such that the prefactor of  $q_{b,\nu_n}$  in Eq. (31) becomes independent of  $\nu_n$ ,

$$\tilde{M}(\nu_n) = \frac{\Delta\tau k + \frac{4m}{\Delta\tau}}{\Delta\tau k + \frac{m}{\Delta\tau} (2 - 2\cos(2\pi\nu_n))}. \quad (34)$$

Although this choice is guided by the non-interacting case  $g = 0$ , we also use it for  $g > 0$  [16]. The modified Langevin equation reads

$$\mathbf{q}(t_l + \delta t_l) = \mathbf{q}(t_l) - \hat{\mathbf{F}}^{-1} \left[ \delta t_l \tilde{M}(\nu_n) \hat{\mathbf{F}} \left[ -\frac{dS}{d\mathbf{q}(t_l)} \right] \right] - \sqrt{2\delta t_l} \sqrt{\tilde{M}(\nu_n)} \hat{\mathbf{F}} [\boldsymbol{\eta}(t_l)]. \quad (35)$$

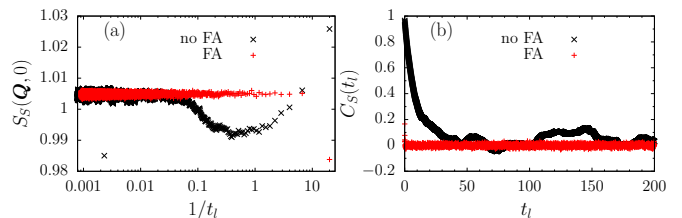


FIG. 4. (a) Equal-time spin correlation function  $S_S(\mathbf{q}, 0)$  and (b) corresponding autocorrelation function  $C_S(t_l)$  at wave vector  $\mathbf{Q}$  as a function of Langevin time  $t_l$  with and without the use of Fourier acceleration (FA). The parameter sets for both runs are exactly the same (including number of sweeps/bins):  $\omega_0 = 0.4$ ,  $L = 6$ ,  $\beta = 7.0$ , and  $\delta t_l = 0.001$ .

To see the effect of Fourier acceleration on autocorrelations, we measured the equal-time spin correlator

$$S_S(\mathbf{q}, 0) = \frac{1}{L^2} \sum_{\mathbf{i}, \mathbf{j}} e^{-i\mathbf{q}(\mathbf{i}-\mathbf{j})} \times \left( \langle \hat{S}_{\mathbf{i},z} \hat{S}_{\mathbf{j},z} \rangle - \langle \hat{S}_{\mathbf{i},z} \rangle \langle \hat{S}_{\mathbf{j},z} \rangle \right) \quad (36)$$

with [using Eq. (35) to update the fields] and without (by setting  $M = 1$ ) Fourier acceleration. Results at wave vector  $\mathbf{Q}$  are shown in Fig. 4(a) as a function of the inverse Langevin time. The equilibration time is obviously reduced by Fourier acceleration and the results of both methods agree at sufficiently long times.

We also consider the autocorrelation function [18]

$$C_{\hat{O}}(t_l) = \sum_{t'_l=0}^{T_l-t_l} \frac{(O(t'_l) - \langle \hat{O} \rangle) (O(t'_l + t_l) - \langle \hat{O} \rangle)}{(O(t'_l) - \langle \hat{O} \rangle)^2}. \quad (37)$$

$O(t_l)$  is the observable evaluated at time  $t_l$  and  $T_l$  is the maximal time at which measurements were taken. Shorter autocorrelation times imply a faster decay of the autocorrelation function. A decrease of autocorrelations by Fourier acceleration is clearly visible in Fig. 4(b).

## IV. RESULTS

The key questions to be addressed are as follows. Starting from the exact mean-field VBS ground state at  $\omega_0 = 0$  (established in Sec. IV A), what is the impact of thermal fluctuations? What happens upon enhancing quantum lattice fluctuations by increasing  $\omega_0$  at fixed electron-phonon coupling? Does the AFM order suggested by the interaction (12), derived for  $\omega_0 = \infty$ , emerge at finite and potentially experimentally relevant phonon frequencies? Are the VBS and AFM phases connected by a single phase transition or via an intermediate metallic phase? Finally, how does the evolution from VBS to AFM order manifest itself in the spectral properties?

Simulations were done for spin-1/2 fermions ( $N = 2$ ) on  $L \times L$  square lattices with mixed boundary conditions,

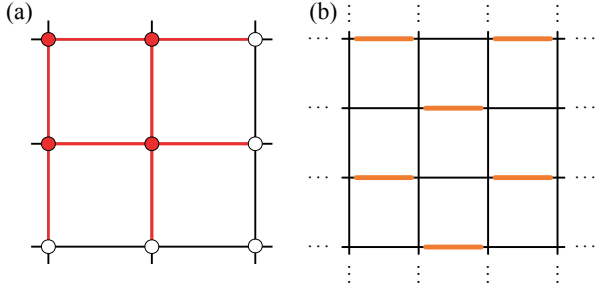


FIG. 5. (a) Unit cell used in mean-field theory, indicated by the colored sites and bonds. (b) Resulting minimal-energy  $(\pi, \pi)$  VBS pattern. Strong bonds are colored while weak bonds are represented by black lines.

see Sec. II. We set  $k = 2$ ,  $t = 1$ ,  $g = 1.5$  and  $\Delta\tau = 0.1$ . The Langevin time step was  $\delta t_l = 0.01$  for  $\omega_0 = 0$  and  $\delta t_l = 0.0005$  else.

All simulations were carried out using the ALF package [18], which provides a generic, high-performance implementation of the AFQMC method as well as tools for stochastic analytic continuation and error analysis. Error bars were obtained using binning analysis [18, 42, 52] and the delete-1 jackknife scheme [18, 52, 53], respectively.

### A. Adiabatic limit

For completeness, we use a mean-field approach to find the minimal energy configuration of the classical fields  $q_b$  and hence the ground state of Eq. (7). The nested Fermi surface of the non-interacting problem gives rise to a log divergence of the  $\mathbf{q} = \mathbf{Q}$  bond susceptibility at low temperatures and hence to a gapped VBS ground state. In contrast to one dimension, where the ordering pattern is unique, possible 2D VBS patterns include staircase, columnar, staggered, and plaquette arrangements [19, 30]. We use a  $2 \times 2$  unit cell and vary the bond variables independently according to the aforementioned symmetry (see Fig. 5(a)), thereby allowing all  $(\pi, \pi)$  and  $(0, \pi)$  patterns. Energy minimization yields the  $(\pi, \pi)$  staggered VBS state illustrated in Fig. 5(b). The same pattern was observed numerically in Ref. [15].

The phonons enhance the hopping amplitude on all bonds and effectively renormalize the electronic bandwidth. Furthermore, they modulate the hopping in a  $(\pi, \pi)$  pattern (see Fig. 5(b)) that leads to a finite gap at the Fermi surface. Since the VBS ordering breaks the discrete  $C_4$  symmetry of the lattice, it can survive at finite temperatures.

To study the thermal melting of the VBS state, we consider the partition function of Hamiltonian (7),

$$Z = \int \prod_b dq_b e^{-S}, \quad (38)$$

$$S = \beta \sum_b \frac{k}{2} q_b^2 - N_\sigma \ln \det \left[ \mathbf{1} + e^{-\beta \sum_b (-t+gq_b) K_b} \right].$$

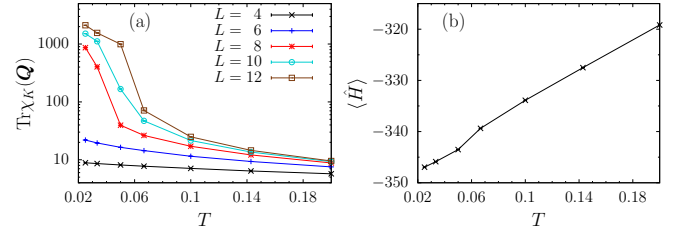


FIG. 6. (a) Bond susceptibility as a function of temperature for different system sizes. (b) Energy as a function of temperature for  $L = 12$ . Simulations were done using  $\delta t_l = 0.01$  and starting from the mean-field configuration.

The determinant is strictly positive since its argument is a symmetric matrix. Therefore, we can use Langevin dynamics without divergences in the forces to update the phonon fields via

$$\frac{\partial S}{\partial q_b} = \beta k q_b + \beta g N \text{Tr} \{ K_b (1 - G) \}, \quad (39)$$

$$G_{i,j} = \frac{\text{Tr} \left[ e^{-\beta \sum_b (-t+gq_b) \hat{K}_b} \hat{c}_i \hat{c}_j^\dagger \right]}{\text{Tr} \left[ e^{-\beta \sum_b (-t+gq_b) \hat{K}_b} \right]}.$$

The onset of VBS order can be captured by the bond-kinetic susceptibility

$$\chi_K^{\delta, \delta'}(\mathbf{q}) = \int_0^\beta d\tau S_K^{\delta, \delta'}(\mathbf{q}, \tau) \quad (40)$$

with the imaginary-time-displaced correlation function

$$S_K^{\delta, \delta'}(\mathbf{q}, \tau) = \left\langle \hat{K}^\delta(\mathbf{q}, \tau) \hat{K}^{\delta'}(-\mathbf{q}) \right\rangle - \left\langle \hat{K}^\delta(\mathbf{q}) \right\rangle \left\langle \hat{K}^{\delta'}(-\mathbf{q}) \right\rangle \quad (41)$$

and

$$\hat{K}^\delta(\mathbf{q}) = \frac{1}{\sqrt{N}} \sum_{i,\sigma} e^{i\mathbf{q} \cdot \mathbf{i}} \left( \hat{c}_{i,\sigma}^\dagger \hat{c}_{i+\mathbf{a}_{\delta,\sigma}} + \text{h.c.} \right). \quad (42)$$

Figure 6 shows results as a function of temperature at the ordering wave vector  $\mathbf{Q}$ . Simulations were started in the mean-field configuration to reduce warm-up times. At low temperatures, the susceptibility grows with increasing  $L$ , signaling long-range VBS order. On our largest lattice size ( $L = 12$ ), we observe a sudden drop of the signal at  $T \approx 0.06$  (see Fig. 6(a)). The energy  $\langle \hat{H} \rangle$  shows a kink at the same temperature [Fig. 6(b)]. Above this critical temperature, thermal fluctuations destroy the long-range order.

## B. Finite phonon frequencies

### 1. Equal-time and static quantities

To map out the phases as a function of phonon frequency, we computed the spin-spin correlations

$$S_S(\mathbf{q}, \tau) = \langle \hat{S}_z(\mathbf{q}, \tau) \hat{S}_z(-\mathbf{q}) \rangle - \langle \hat{S}_z(\mathbf{q}, \tau) \rangle \langle \hat{S}_z(-\mathbf{q}) \rangle, \quad (43)$$

as well as the imaginary-time-displaced correlations of the bond-kinetic energy defined in Eq. (41). Here,

$$\hat{S}_z(\mathbf{q}) = \frac{1}{\sqrt{N}} \sum_i e^{i\mathbf{q}\cdot\mathbf{i}} (\hat{n}_{i,\uparrow} - \hat{n}_{i,\downarrow}). \quad (44)$$

We also considered the bond-kinetic susceptibility of Eq. (40) and the equivalent form of the spin susceptibility,  $\chi_S(\mathbf{q})$ . Because of the O(4) symmetry of Eq. (1), see Sec. II, the three components of the spin-spin correlations are degenerate with CDW and s-wave SC correlations. Here, we will discuss the results from the point of view of spin-spin correlations.

In Fig. 7, we present the dependence of the bond-kinetic susceptibility and structure factor on lattice size, temperature, and phonon frequency. At the lowest frequency considered ( $\omega_0 = 0.4$ ),  $\text{Tr} \chi_K(\mathbf{Q})$  grows as a function of size and inverse temperature, suggesting the same  $(\pi, \pi)$  VBS order as in the adiabatic limit. Note that the lowest temperature,  $T = 1/40$ , was not sufficient to achieve convergence of  $\text{Tr} \chi_K(\mathbf{Q})$  for  $L = 12$ . Contrary to theoretical expectations based on the log divergence caused by Fermi surface nesting, a nonzero critical value for VBS order was reported in Ref. [15] for  $\omega_0 = 1$ . While the limitations regarding system size do not allow us to address this contradiction, our observation of VBS order at the dimensional coupling  $\lambda = g^2/8kt = 0.141$  and for

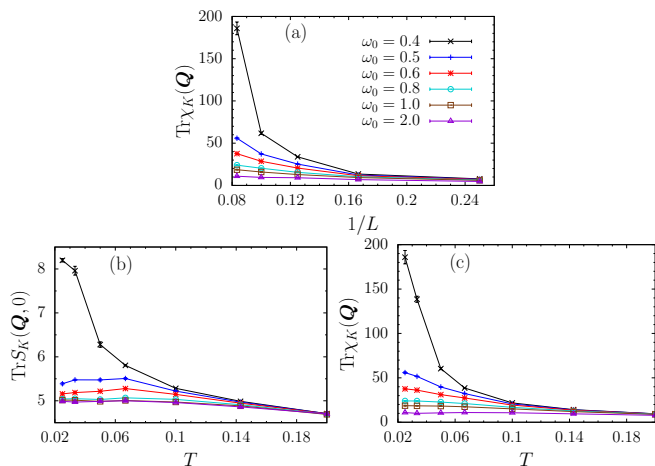


FIG. 7. (a) Finite-size scaling of the bond-kinetic susceptibility at  $T = 1/40$ . (b) Temperature dependence of the bond-kinetic structure factor and (c) of the bond-kinetic susceptibility for  $L = 12$ .

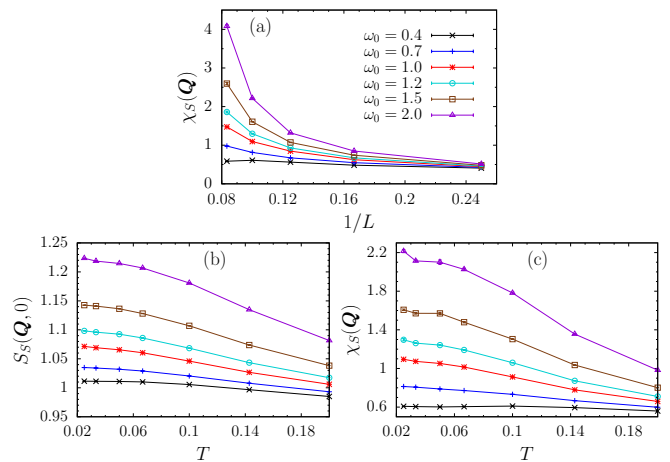


FIG. 8. (a) Finite-size scaling of the spin susceptibility at  $T = 1/40$ . (b) Temperature dependence of the spin structure factor for  $L = 10$ . (c) Temperature dependence of the spin susceptibility for  $L = 10$ .

$\omega_0 = 0.4$  is compatible with VBS order for  $\lambda \gtrsim 0.112$  and  $\omega_0 = 1$  in Ref. [15]. As  $\omega_0$  is increased, we observe a rapid drop in  $\text{Tr} \chi_K(\mathbf{Q})$  that indicates that the VBS state gives way to another phase.

In Fig. 8(a), we show results for the spin degrees of freedom. At low temperatures, the size-dependence of the AFM spin susceptibility shows a marked increase at *high* phonon frequencies. In Figs. 8(b) and (c), the temperature dependence at fixed lattice size shows that we are able to achieve convergence with respect to temperature. This allows us to compute the correlation ratio

$$R_{\chi,S} = 1 - \frac{\chi_S(\mathbf{Q} + \Delta\mathbf{q})}{\chi_S(\mathbf{Q})} \quad (45)$$

where  $|\Delta\mathbf{q}| = 2\pi/L$ . This renormalization group invariant quantity takes the value of unity (zero) in the ordered (disordered) phase. At  $T = 0$  and for a continuous transition, it scales as

$$R_{\chi,S} = f\left([\omega_0 - \omega_0^c]L^{1/\nu}\right). \quad (46)$$

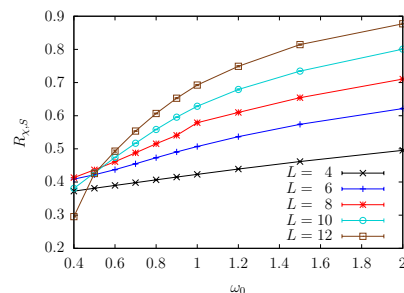


FIG. 9. Correlation ratio based on the spin susceptibility as defined in Eq. (45). Here,  $T = 1/40$ , which is representative of the ground state for this quantity.



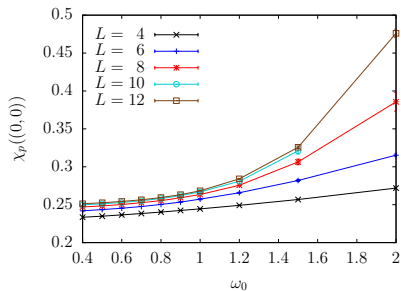


FIG. 10. Parity susceptibility [Eq. (47)] at  $T = 0.1$ .

Figure 9 shows  $R_{\chi,S}$  as a function of system size for the lowest temperature available (representative of the ground state). Although corrections to scaling, not included in Eq. (46), lead to a drift of the crossing points, the data suggest a critical phonon frequency  $\omega_0^c \simeq 0.6$  for the onset of long-range AFM order.

Being a modulation of the bond-kinetic energy, the VBS state does not break the underlying  $O(4)$  symmetry of the lattice. However, it does break translation and rotation symmetries. On the other hand, the AFM phase does break the  $O(4)$  symmetry, as can be demonstrated by computing the susceptibility of the parity operator defined in Eq. (3),

$$\chi_p(\mathbf{q}) = \int_0^\beta d\tau \sum_{\mathbf{r}} e^{i\mathbf{q}\cdot\mathbf{r}} \langle \hat{p}_{\mathbf{r}}(\tau) \hat{p}_{\mathbf{0}} \rangle. \quad (47)$$

Since  $\hat{p}_i$  is an Ising variable that changes sign under an  $O(4)$  transformation  $\mathcal{M}$  with  $\det \mathcal{M} = -1$ , we expect  $\chi_p(\mathbf{0})$  to diverge at a critical temperature associated with a phase transition in the 2D Ising universality class. Being an 8-point correlation function,  $\chi_p(\mathbf{q})$  becomes very noisy at low temperatures and we are restricted to  $T = 0.1$ . Figure 10 shows results as a function of system size and phonon frequency. For  $\omega_0 = 2$ ,  $\chi_p(\mathbf{0})$  grows with increasing  $L$ , suggesting that for this frequency the Ising temperature is below  $T = 0.1$ . On the other hand, for  $\omega_0 = 1$  (still in the AFM phase) our temperature is too high to capture the Ising transition. We conclude that the AFM phase breaks the  $O(4)$  symmetry down to  $SO(4)$  at a finite-temperature Ising transition occurring at  $T_c^I$ . A natural conjecture is that  $T_c^I$  vanishes at  $\omega_0^c$ .

## 2. Dynamical quantities

To extract spectral functions from QMC data for imaginary-time correlators via analytic continuation, we used the ALF implementation [18] of the stochastic maximum entropy algorithm [54, 55].

The single-particle spectral function  $A(\mathbf{k}, \omega)$ , accessible in ARPES experiments, is related to the imaginary-

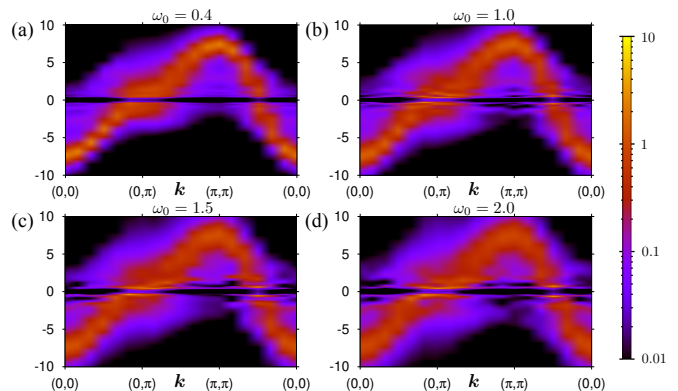


FIG. 11. Single-particle spectral function  $A(\mathbf{k}, \omega)$  for different phonon frequencies. Here,  $L = 12$ ,  $\beta = 40$ .

time Green function via

$$\langle \hat{c}_{\mathbf{k},\sigma}(\tau) \hat{c}_{\mathbf{k},\sigma}^\dagger(0) \rangle = \frac{1}{\pi} \int d\omega \frac{e^{-\tau\omega}}{1 + e^{-\beta\omega}} A(\mathbf{k}, \omega). \quad (48)$$

Figure 11(a) shows  $A(\mathbf{k}, \omega)$  for  $\beta = 40$  and  $L = 12$ . The coupling of the Einstein phonon mode to the electrons breaks the  $\hat{Q}_b \rightarrow -\hat{Q}_b$  symmetry. Consequently,  $\frac{1}{2N} \sum_b \langle \hat{Q}_b \rangle$  acquires a non-zero expectation value that renormalizes the electronic bandwidth. For  $\omega_0 = 0.4$ ,  $\frac{1}{2N} \sum_b \langle \hat{Q}_b \rangle = -0.56510(7)$ , yielding an effective hopping  $t_{\text{eff}} = 1.85$ . This explains the observed range of the band from  $-4t_{\text{eff}}$  at  $\mathbf{k} = (0, 0)$  to  $4t_{\text{eff}}$  at  $\mathbf{k} = (\pi, \pi)$ . For  $\omega_0 = 0.4$ , inside the VBS phase, the  $(\pi, \pi)$  modulation of the hopping opens a gap at the non-interacting Fermi surface, as visible for  $\mathbf{k} = (0, \pi)$  and  $\mathbf{k} = (\pi/2, \pi/2)$  in Fig. 11(a). Both, the gap and the cosine band of width  $8t_{\text{eff}}$  are features that can be qualitatively accounted for at the mean-field level. However, the spectral function exhibits low-lying spectral weight that extends over the considered path in the Brillouin zone. In analogy with the 1D Holstein model [56], and guided by the results of a self-consistent Born approximation shown below, we attribute this low-energy feature to polaron formation. The  $O(4)$  symmetry of the model implies  $A(\mathbf{k}, \omega) = A(\mathbf{k} + \mathbf{Q}, -\omega)$ . Hence, in the absence of symmetry breaking, the polaron band is nested and should exhibit instabilities to AFM or VBS order.

Figure 12 shows the single-particle spectral function from a self-consistent Born approximation (see appendix). In the latter, we neglect phonon renormalization and instead use an effective hopping  $t = 1.85$  derived from the QMC data. Figure 12(a) reveals a cosine band with a gap of the order of the bare phonon frequency  $\omega_0$  that is crossed by a narrow polaron band. A full gap—as in the QMC data—is achieved within this approximation by an additional single-particle term

$$\hat{H}_\lambda = \lambda \sum_i e^{i\mathbf{Q}i} (\hat{n}_{i,\uparrow} - \hat{n}_{i,\downarrow}) \quad (49)$$

that explicitly breaks the  $O(4)$  symmetry by enforcing AFM order, see Fig. 12(b). The Born approximation

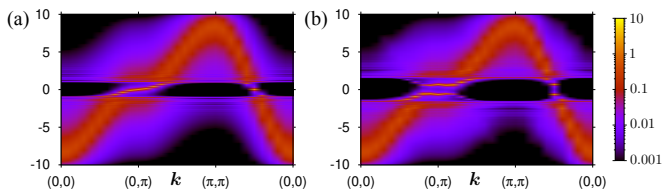


FIG. 12. (a) Single-particle spectral function  $A(\mathbf{k}, \omega)$  from a self-consistent Born approximation for  $\beta = 40$ ,  $t = 1.85$ ,  $g = 1.5$ ,  $\omega_0 = 1.0$ . (b) As in (a) but with broken  $O(4)$  symmetry via addition of  $\hat{H}_\lambda$  [Eq. (49)] with  $\lambda = 0.5$ .

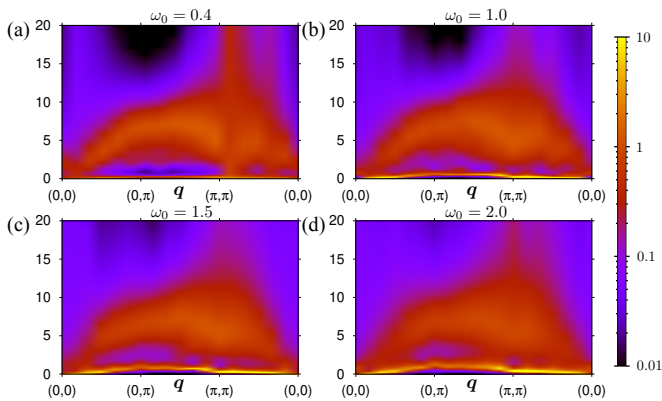


FIG. 13. VBS dynamical structure factor  $S_K(\mathbf{q}, \omega)$  for different phonon frequencies. Here,  $L = 12$ ,  $\beta = 40$ .

provides a qualitative interpretation of the features observed numerically but—as expected—does not capture quantitative aspects such as the true size of the gaps.

Upon increasing the phonon frequency to  $\omega_0 = 2$ , Figs. 11(b)-(d),  $\frac{1}{2N} \sum_b \langle \hat{Q}_b \rangle$  remains almost constant and, consequently, the width of the cosine band does not change substantially. However, we observe a transfer of spectral weight to the polaron band. The origin of the gap at  $\omega_0 > \omega_0^c$  is to be found in AFM ordering. Our QMC data suggest that the single-particle gap remains open across the VBS-AFM transition.

Figure 13 shows the VBS dynamical structure factor  $S_K(\mathbf{q}, \omega)$  at four different phonon frequencies. We computed the imaginary part of the dynamical VBS susceptibility  $\text{Tr}\chi''_K(\mathbf{q}, \omega)$  by using the maximum entropy method

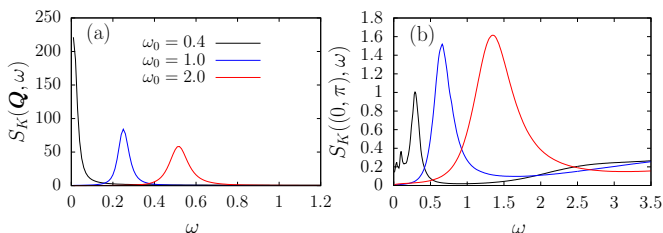


FIG. 14. VBS dynamical structure factor for (a)  $\mathbf{q} = \mathbf{Q}$  and (b)  $\mathbf{q} = (0, \pi)$  for different  $\omega_0$ . Here,  $L = 12$ ,  $\beta = 40$ .

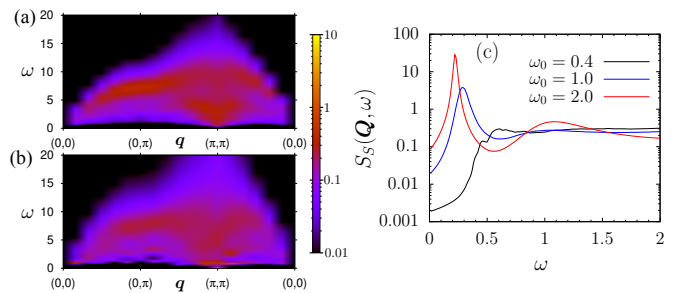


FIG. 15. Spin dynamical structure factor  $S_S(\mathbf{q}, \omega)$  for (a)  $\omega_0 = 0.4$ , (b)  $\omega_0 = 2.0$ , (c) fixed  $\mathbf{q} = \mathbf{Q}$  and different  $\omega_0$ . Here,  $L = 12$ ,  $\beta = 40$ .

[18] to invert

$$\text{Tr}S_K(q, \tau) = \frac{1}{\pi} \int d\omega \frac{e^{-\tau\omega}}{1 - e^{-\beta\omega}} \text{Tr}\chi''_K(q, \omega). \quad (50)$$

The dynamical VBS structure factor then follows from

$$S_K(\mathbf{q}, \omega) = \frac{\text{Tr}\chi''_K(\mathbf{q}, \omega)}{(1 - e^{-\beta\omega})}. \quad (51)$$

Since the phonons couple to the bond-kinetic energy,  $S_K(\mathbf{q}, \omega)$  should reveal both the phonon dynamics and the particle-hole continuum. At  $\omega_0 = 0.4$  (Fig. 13(a)), we see substantial, very low-lying weight as well as high-energy features that reflect the particle-hole continuum. The low-lying excitation corresponds to the phonon mode. The fact that it is soft at  $\mathbf{q} = \mathbf{Q}$  is a signature of long-range VBS order. In Fig. 14 we show  $S_K(\mathbf{q}, \omega)$  at wave vector  $\mathbf{Q}$  and also at  $\mathbf{q} = (0, \pi)$  for comparison. However, we cannot resolve the dispersion relation. In comparison to the bandwidth, the renormalized phonon modes are very slow and are at the origin of long auto-correlation times. In the AFM phase, Figs. 13(c)-(d), the phonon mode acquires a gap.

Finally, we show the dynamical spin structure factor

$$S_S(\mathbf{q}, \omega) = \frac{\text{Tr}\chi''_S(\mathbf{q}, \omega)}{(1 - e^{-\beta\omega})}. \quad (52)$$

in Fig. 15. Because phonons do not carry spin, they are not visible in spin-flip scattering processes. According to Fig. 15(a), in the VBS phase,  $S_S(\mathbf{q}, \omega)$  is dominated by the particle-hole continuum. For  $\omega_0 \geq 1.0$ , low-energy spectral weight at  $\mathbf{q} = \mathbf{Q}$  reflects long-range AFM order, see Figs. 15(b)-(c).

## V. DISCUSSION AND CONCLUSIONS

Our results provide both algorithmic and physical insights into the fundamental 2D SSH model.

### A. Langevin dynamics

We used a Langevin dynamics updating scheme with Fourier acceleration [16] in the framework of the auxiliary-field quantum Monte Carlo method.

In contrast to the HMC approach in Ref. [26], we computed forces exactly for a given field configuration. A comparison between stochastic and deterministic calculations of forces can be found in Ref. [57]. Although the CPU time per sweep is longer and scales as  $L^6\beta$ , fluctuations, especially for time-displaced correlation functions, are smaller.

One of the key difficulties encountered in Langevin dynamics are zeros of the determinant, which lead to logarithmic singularities of the action. Exploiting the  $O(4)$  symmetry of the SSH model, the determinant can be written as the square of a Pfaffian, whose average sign provides a measure for the density of zeros of the determinant. We demonstrated that for *low* phonon frequencies, the density is small, so that Langevin simulations can be stabilized using an adaptive time step scheme. Nevertheless, simulations occasionally suffer from spikes in observables when the stochastic walk approaches a zero. Obviously, such configurations have very small weight and a hybrid molecular dynamics update may be more efficient. In principle, the resulting ergodicity issues can be overcome by a *complexification* of the fields [26]. For the Hubbard model, this is possible since the decoupling of the interaction can be done in various channels. For the SSH model, we do not have such liberty.

We find that global Langevin updates are a good choice in the adiabatic regime where local moves fail. As the phonon frequency grows, Langevin dynamics becomes increasingly challenging. At the same time, local updates become favorable, as discussed, e.g., in Ref. [58].

### B. Physics of the 2D SSH model

Despite its apparent simplicity and fundamental nature, remarkably little was known about the 2D SSH model. The existence and type of long-range VBS order was settled only recently [15]. Our results elucidate the physics of the SSH model at a fixed electron-phonon coupling and as a function of the phonon frequency. In addition to static observables, we specifically also presented excitation spectra from QMC and analytical methods. The numerical results were further complemented with a mean-field approach to the VBS phase and simulations showing the temperature-driven destruction of VBS order in the adiabatic limit.

The features of the phase diagram in Fig. 1 are tied to the  $O(4)$  symmetry of the model. In particular, the single-particle spectral function satisfies  $A(\mathbf{k}, \omega) = A(\mathbf{k} + \mathbf{Q}, -\omega)$ . Hence, any Fermi liquid state that does not break this symmetry will ultimately be unstable to orders that can open up a gap. This includes the  $\mathbf{Q} = (\pi, \pi)$  VBS phase as well as AFM order. In the

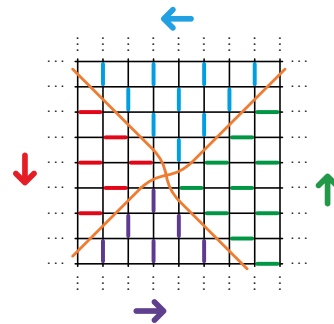


FIG. 16. A vortex of the  $(\pi, \pi)$  VBS state. Arrows represent the four degenerate VBS patterns that break the  $C_4$  symmetry. By crossing a domain wall (orange lines), the angle changes by  $\pi/2$ . A full circle around the core yields  $2\pi$ . This *trivial* vortex does not carry a spin-1/2 degree of freedom, in contrast to the case of  $(0, \pi)$  or  $(\pi, 0)$  VBS orders [59].

adiabatic limit, the problem simplifies since the phonons become classical and mean-field theory gives a  $(\pi, \pi)$  VBS phase as the exact ground state. For  $\omega_0 > 0$ , the phonons can be integrated out in favor of a retarded interaction. The latter reduces to Eq. (12) in the antiadiabatic limit  $\omega_0 \rightarrow \infty$ , where it triggers an AFM state that is degenerate with CDW and SC states. Two key results are the existence of AFM order down to the experimentally relevant adiabatic regime  $\omega_0 < t$  and a direct transition from VBS to AFM order. The single-particle spectral function supports the picture of a narrow polaronic band undergoing a transition from a  $(\pi, \pi)$  VBS to AFM/CDW/SC. In the particle-hole channel, the dynamical VBS correlation function reveals the phonon dynamics as a function of decreasing phonon frequency, including a softening at  $(\pi, \pi)$ . On the other hand, as  $\omega_0$  grows, we observe enhanced spectral weight at low energies and at  $\mathbf{q} = \mathbf{Q}$  in the spin channel.

The VBS phase breaks lattice symmetries but not the above  $O(4)$  symmetry. On the other hand, AFM or SC/CDW phases break the  $O(4)$  symmetry down to  $SU(2)$  but leave lattice symmetries in tact. Starting at high temperatures, the symmetry reduction to  $SU(2)$  occurs in two steps. At a critical temperature, spontaneous ordering of the parity operator takes place at an Ising transition. Even parity corresponds to the SC/CDW phase, odd parity to the AFM phase. Then, at  $T = 0$ , the  $SU(2)$  spin (pseudospin) symmetry is spontaneously broken, leaving the  $SU(2)$  pseudospin (spin) symmetry unbroken.

Generically, the  $O(4)$  symmetry will be broken down to  $SU(2)$  by, for example, adding a next-nearest-neighbor hopping. In this case, we expect the phase diagram to be dominated by superconductivity, as the Cooper instability is insensitive to the shape of the Fermi surface. The stability of the VBS phase as a function of an  $O(4)$  symmetry-breaking interaction such as a chemical potential or a next-nearest-neighbor hopping deserves a detailed investigation.

The nature of the VBS-AFM transition remains elusive. Because it occurs between states with different symmetries, Ginzburg-Landau order parameter theory generically predicts either a first-order transition or a region of coexistence. Within the  $\omega_0$  resolution of our results, this was not observed. Instead, the transition appears continuous. The theory of deconfined quantum critical points (DQCPs) [60, 61] does not apply. To see this, we can adopt the DQCP picture of an 8-component Dirac metal with five anti-commuting AFM and VBS mass terms [62–64]. The algebra of the mass terms guarantees that the core of a vortex in the VBS order parameter carries a spin-1/2 excitation. However, this requires an ordering wavevector  $(0, \pi)$  or  $(\pi, 0)$ . In contrast, the  $(\pi, \pi)$  VBS observed here does not correspond to a Dirac mass term. This point of view is substantiated by noticing that a  $C_4$  vortex of the  $(\pi, \pi)$  VBS can be trivial, as explained in Fig. 16. Finally, a deconfined VBS-CDW phase transition as a function of phonon frequency exists in the spinless 1D SSH model [36], whereas long-range AFM order is ruled out in 1D models by the Mermin-Wagner theorem.

In summary, we have established the existence of a  $(\pi, \pi)$ -ordered VBS phase and an AFM phase in the 2D SSH model with quantum phonons by means of QMC simulations. Notably, the AFM phase exists even at finite phonon frequencies. We observed an apparently direct transition between these phases with no signatures of an intermediate metallic region. Finally, we provided an interpretation of the numerical results for the single-particle spectral function in terms of gap formation in a narrow polaronic band.

*Note added:* During the preparation of this article we became aware of Ref. [65], the results of which appear to be fully consistent with ours. While the authors do not present excitation spectra, they provide a phase diagram with critical values for multiple parameter sets based on larger lattice sizes than the present work. Nevertheless, our critical value  $\omega_0^c \approx 0.6$  for the dimensionless coupling constant  $\lambda = g^2/8kt \approx 0.141$  is in satisfactory agreement with their phase boundary. Moreover, Ref. [65] also points out that the critical coupling for VBS order is expected to vanish in the 2D SSH model, in contrast to the findings of Ref. [15]. Finally, the authors of Ref. [65] provide similar arguments regarding the properties of vortices of the VBS pattern and its implications for the interpretation of the VBS-AFM transition.

## ACKNOWLEDGMENTS

We thank E. Huffman for helpful discussions on the calculation of the Pfaffian and F. Goth for discussions on related work. The authors gratefully acknowledge the Gauss Centre for Supercomputing e.V. (www.gauss-centre.eu) for funding this project by providing computing time on the GCS Supercomputer SUPERMUC-NG at Leibniz Supercomputing Centre (www.lrz.de). FFA

thanks the Würzburg-Dresden Cluster of Excellence on Complexity and Topology in Quantum Matter ct.qmat (EXC 2147, project-id 390858490), AG and SB the DFG funded SFB 1170 on Topological and Correlated Electronics at Surfaces and Interfaces.

## Appendix: Self-consistent Born approximation

The Dyson equation for the full Green function is

$$G(\mathbf{k}, i\omega_m) = [G_0^{-1}(\mathbf{k}, i\omega_m) - \Sigma(\mathbf{k}, i\omega_m)]^{-1} \quad (\text{A.1})$$

with the non-interacting Green function  $G_0$  and fermionic Matsubara frequencies  $\omega_m$ . Here, we only consider the Fock contribution to the electron self energy,

$$\Sigma = \text{---} \text{---} \text{---} + \dots,$$

where the wavy line represents the non-interacting phonon propagator  $D_0$  and the double line the full Green function  $G$ . The contribution of this Feynman diagram is given by [66, 67]

$$\Sigma(\mathbf{k}, i\omega_m) = -\frac{1}{\beta} \sum_{i\omega_n} \sum_{\mathbf{q}, \delta} \left| g_{\mathbf{k}+\mathbf{q}, \mathbf{k}}^{\mathbf{q}, \delta} \right|^2 G(\mathbf{k} + \mathbf{q}, i\omega_n) D_0(i\omega_n - i\omega_m), \quad (\text{A.2})$$

to be solved self-consistently together with Eq. (A.1).

The matrix elements  $g_{\mathbf{k}+\mathbf{q}, \mathbf{k}}^{\mathbf{q}, \delta}$  are defined by the electron-phonon interaction in Hamiltonian (1), which can be expressed after Fourier transformation as

$$\hat{H}_{\text{ep}} = \sum_{\mathbf{k}, \mathbf{q}, \sigma} \sum_{\delta} g_{\mathbf{k}+\mathbf{q}, \mathbf{k}}^{\mathbf{q}, \delta} \hat{c}_{\mathbf{k}+\mathbf{q}, \sigma}^{\dagger} \hat{c}_{\mathbf{k}, \sigma} \left( \hat{d}_{-\mathbf{q}, \delta}^{\dagger} + \hat{d}_{\mathbf{q}, \delta} \right),$$

$$g_{\mathbf{k}+\mathbf{q}, \mathbf{k}}^{\mathbf{q}, \delta} = \frac{g}{\sqrt{2m\omega_0 N}} \left( e^{-i(\mathbf{k}+\mathbf{q}/2)\delta} + e^{i(\mathbf{k}+\mathbf{q}/2)\delta} \right). \quad (\text{A.3})$$

Here, we have rewritten the position operator of the phonons in terms of bosonic creation and annihilation operators,  $\hat{Q}_b = \frac{1}{\sqrt{2m\omega_0}} \left( \hat{d}_b^{\dagger} + \hat{d}_b \right)$ . The vector  $\delta$  connects two nearest-neighbor sites,  $b = \langle \mathbf{i}, \mathbf{i} + \delta \rangle$ . The non-interacting phonon propagator can be written as

$$D_0(i\Omega_m) = \frac{1}{i\Omega_m - \omega_0} - \frac{1}{i\Omega_m + \omega_0}, \quad (\text{A.4})$$

where  $\Omega_m$  is a bosonic Matsubara frequency. To carry out the summation over the Matsubara frequencies in Eq. (A.2), we rewrite the Green function with the spectral function  $A(\mathbf{k}, \omega) = -(1/\pi)\text{Im} G^{\text{R}}(\mathbf{k}, \omega)$ ,

$$G(\mathbf{k}, i\omega_m) = \int d\omega \frac{A(\mathbf{k}, \omega)}{i\omega_m - \omega}, \quad (\text{A.5})$$

where the retarded Green function  $G^{\text{R}}(\mathbf{k}, \omega) = G(\mathbf{k}, i\omega_m \rightarrow \omega + i\varepsilon)$  is obtained by analytical continuation

with an infinitesimal  $\varepsilon$ . We obtain for the self-energy [56]

$$\Sigma(\mathbf{k}, \omega + i\varepsilon) = \int d\bar{\omega} \sum_{\mathbf{q}, \delta} \left| g_{\mathbf{k}+\mathbf{q}, \mathbf{k}}^{\mathbf{q}, \delta} \right|^2 A(\mathbf{k} + \mathbf{q}, \bar{\omega}) \times \left[ \frac{n_B(\omega_0) + n_F(\bar{\omega})}{\omega + i\varepsilon + \omega_0 - \bar{\omega}} + \frac{n_B(\omega_0) + 1 - n_F(\bar{\omega})}{\omega + i\varepsilon - \omega_0 - \bar{\omega}} \right]. \quad (\text{A.6})$$

Here,  $n_B(\omega_0) = \frac{1}{e^{\beta\omega_0} - 1}$  and  $n_F(\omega) = \frac{1}{e^{\beta\omega} + 1}$  are the Bose-Einstein and Fermi-Dirac distributions respectively.

Our approximation neglects the renormalization of the phonons due to the electrons and vertex corrections.

- 
- [1] J. Bardeen, L. N. Cooper, and J. R. Schrieffer, Theory of superconductivity, *Phys. Rev.* **108**, 1175 (1957).
- [2] M. Hohenadler and H. Fehske, Density waves in strongly correlated quantum chains, *Eur. Phys. J. B* **91**, 204 (2018).
- [3] M. Weber, Valence bond order in a honeycomb antiferromagnet coupled to quantum phonons, *Phys. Rev. B* **103**, L041105 (2021).
- [4] A. Migdal, Interaction between electrons and lattice vibrations in a normal metal, *JETP* **34**, 996 (1958).
- [5] I. Esterlis, B. Noszarzewski, E. W. Huang, B. Moritz, T. P. Devereaux, D. J. Scalapino, and S. A. Kivelson, Breakdown of the migdal-eliasberg theory: A determinant quantum monte carlo study, *Phys. Rev. B* **97**, 140501 (2018).
- [6] C. Wu and S.-C. Zhang, Sufficient condition for absence of the sign problem in the fermionic quantum monte carlo algorithm, *Phys. Rev. B* **71**, 155115 (2005).
- [7] F. F. Assaad and T. C. Lang, Diagrammatic determinantal quantum monte carlo methods: Projective schemes and applications to the hubbard-holstein model, *Phys. Rev. B* **76**, 035116 (2007).
- [8] C. Chen, X. Y. Xu, Z. Y. Meng, and M. Hohenadler, Charge-density-wave transitions of dirac fermions coupled to phonons, *Phys. Rev. Lett.* **122**, 077601 (2019).
- [9] S. Karakuzu, K. Seki, and S. Sorella, Solution of the sign problem for the half-filled hubbard-holstein model, *Phys. Rev. B* **98**, 201108 (2018).
- [10] M. Hohenadler and T. C. Lang, Autocorrelations in quantum monte carlo simulations of electron-phonon models, in *Computational Many-Particle Physics*, edited by H. Fehske, R. Schneider, and A. Weisse (Springer-Verlag Berlin Heidelberg, 2008) pp. 357–366.
- [11] C. Chen, X. Y. Xu, J. Liu, G. Batrouni, R. Scalettar, and Z. Y. Meng, Symmetry-enforced self-learning monte carlo method applied to the holstein model, *Phys. Rev. B* **98**, 041102 (2018).
- [12] T. Holstein, Studies of polaron motion, *Annal. Phys.* **8**, 325 (1959).
- [13] W. P. Su, J. R. Schrieffer, and A. J. Heeger, Soliton excitations in polyacetylene, *Phys. Rev. B* **22**, 2099 (1980).
- [14] M. Hohenadler and G. G. Batrouni, Dominant charge density wave correlations in the holstein model on the half-filled square lattice, *Phys. Rev. B* **100**, 165114 (2019).
- [15] B. Xing, W.-T. Chiu, D. Poletti, R. T. Scalettar, and G. Batrouni, Quantum monte carlo simulations of the 2d su-schrieffer-heeger model, *Phys. Rev. Lett.* **126**, 017601 (2021).
- [16] G. G. Batrouni and R. T. Scalettar, Langevin simulations of a long-range electron-phonon model, *Phys. Rev. B* **99**, 035114 (2019).
- [17] R. Blankenbecler, D. J. Scalapino, and R. L. Sugar, Monte carlo calculations of coupled boson-fermion systems., *Phys. Rev. D* **24**, 2278 (1981).
- [18] ALF Collaboration, F. F. Assaad, M. Bercx, F. Goth, A. Götz, J. S. Hofmann, E. Huffman, Z. Liu, F. Parisen Toldin, J. S. E. Portela, and J. Schwab, The ALF (Algorithms for Lattice Fermions) project release 2.0. Documentation for the auxiliary-field quantum Monte Carlo code, arXiv:2012.11914 (2021), <https://arxiv.org/abs/2012.11914> [cond-mat.str-el].
- [19] S. Tang and J. E. Hirsch, Peierls instability in the two-dimensional half-filled hubbard model, *Phys. Rev. B* **37**, 9546 (1988).
- [20] J. N. Liu, X. Sun, R. T. Fu, and K. Nasu, Effect of electron interaction on the two-dimensional peierls instability, *Phys. Rev. B* **46**, 1710 (1992).
- [21] Yuan, Q., Nunner, T., and Kopp, T., Imperfect nesting and peierls instability for a two-dimensional tight-binding model, *Eur. Phys. J. B* **22**, 37 (2001).
- [22] Q. Yuan and T. Kopp, Coexistence of the bond-order wave and antiferromagnetism in a two-dimensional half-filled peierls-hubbard model, *Phys. Rev. B* **65**, 085102 (2002).
- [23] S. Chiba and Y. Ono, Bow-sdw transition in the two-dimensional peierls-hubbard model, *J. Phys. Soc. Jpn.* **73**, 2777 (2004), <https://doi.org/10.1143/JPSJ.73.2777>.
- [24] S. Beyl, *Hybrid Quantum Monte Carlo for Condensed Matter Models*, Doctoral thesis, Universität Würzburg (2020).
- [25] F. F. Assaad and T. Grover, Simple fermionic model of deconfined phases and phase transitions, *Phys. Rev. X* **6**, 041049 (2016).
- [26] S. Beyl, F. Goth, and F. F. Assaad, Revisiting the hybrid quantum monte carlo method for hubbard and electron-phonon models, *Phys. Rev. B* **97**, 085144 (2018).
- [27] Z.-X. Li, Y.-F. Jiang, and H. Yao, Majorana-time-reversal symmetries: A fundamental principle for sign-problem-free quantum monte carlo simulations, *Phys. Rev. Lett.* **117**, 267002 (2016).
- [28] P. W. Anderson, Random-phase approximation in the theory of superconductivity, *Phys. Rev.* **112**, 1900 (1958).
- [29] J. W. Negele and H. Orland, *Quantum Many-particle Systems* (Westview Press, 1998).
- [30] S. Mazumdar, Valence-bond approach to two-dimensional broken symmetries: Application to  $\text{la}_2\text{cuo}_4$ , *Phys. Rev. B* **36**, 7190 (1987).
- [31] S. Mazumdar, Comment on "peierls instability in the two-dimensional half-filled hubbard model", *Phys. Rev.*

- B **39**, 12324 (1989).
- [32] S. Tang and J. E. Hirsch, Reply to "comment on 'peierls instability in the two-dimensional half-filler hubbard model'", Phys. Rev. B **39**, 12327 (1989).
- [33] Y. Ono and T. Hamano, Peierls distortion in two-dimensional tight-binding model, J. Phys. Soc. Jpn. **69**, 1769 (2000), <https://doi.org/10.1143/JPSJ.69.1769>.
- [34] S. Chiba and Y. Ono, Multi mode phonon softening in two-dimensional electron-lattice system, J. Phys. Soc. Jpn. **72**, 1995 (2003), <https://doi.org/10.1143/JPSJ.72.1995>.
- [35] S. Chiba and Y. Ono, Phonon dispersion relations in two-dimensional peierls phase, J. Phys. Soc. Jpn. **73**, 2473 (2004), <https://doi.org/10.1143/JPSJ.73.2473>.
- [36] M. Weber, F. Parisen Toldin, and M. Hohenadler, Competing orders and unconventional criticality in the suschrieffer-heeger model, Phys. Rev. Research **2**, 023013 (2020).
- [37] K. Ji, K. Iwano, and K. Nasu, Quantum monte carlo study on electron-phonon coupling in monolayer graphene, Journal of Electron Spectroscopy and Related Phenomena **181**, 189 (2010).
- [38] S. Li and S. Johnston, Quantum monte carlo study of lattice polarons in the two-dimensional three-orbital suschrieffer-heeger model, npj Quantum Materials **5**, 1 (2020).
- [39] C. Gardiner, *Stochastic Methods* (Springer, Berlin, Heidelberg, 2009).
- [40] G. G. Batrouni, G. R. Katz, A. S. Kronfeld, G. P. Lepage, B. Svetitsky, and K. G. Wilson, Langevin simulations of lattice field theories, Phys. Rev. D **32**, 2736 (1985).
- [41] W. K. Hastings, Monte carlo sampling methods using markov chains and their applications, Biometrika **57**, 97 (1970).
- [42] W. Krauth, *Statistical Mechanics: Algorithms and Computations* (Oxford University Press, 2006).
- [43] S. R. White and J. W. Wilkins, Fermion simulations in systems with negative weights, Phys. Rev. B **37**, 5024 (1988).
- [44] F. F. Assaad, Quantum monte carlo simulations of the two dimensional single band hubbard model, Helv. Physica Acta **63**, 580 (1990).
- [45] A. N. Rubtsov, V. V. Savkin, and A. I. Lichtenstein, Continuous-time quantum monte carlo method for fermions, Phys. Rev. B **72**, 035122 (2005).
- [46] M. Weber, F. F. Assaad, and M. Hohenadler, Excitation spectra and correlation functions of quantum suschrieffer-heeger models, Phys. Rev. B **91**, 245147 (2015).
- [47] Z.-X. Li, Y.-F. Jiang, and H. Yao, Solving the fermion sign problem in quantum monte carlo simulations by majorana representation, Phys. Rev. B **91**, 241117 (2015).
- [48] E. Huffman, Fermion bag approach for hamiltonian lattice field theories (2018), [arXiv:1912.11776](https://arxiv.org/abs/1912.11776) [cond-mat.str-el].
- [49] M. Wimmer, Algorithm 923, ACM Transactions on Mathematical Software **38**, 30 (2012).
- [50] E. Huffman and S. Chandrasekharan, Fermion-bag inspired hamiltonian lattice field theory for fermionic quantum criticality, Phys. Rev. D **101**, 074501 (2020).
- [51] C. Davies, G. Batrouni, G. Katz, A. Kronfeld, P. Lepage, P. Rossi, B. Svetitsky, and K. Wilson, Langevin simulations of lattice field theories using fourier acceleration, J. Stat. Phys. **43**, 1073 (1986).
- [52] J. Gubernatis, N. Kawashima, and P. Werner, *Quantum Monte Carlo Methods: Algorithms for Lattice Models* (Cambridge University Press, Cambridge, 2016).
- [53] B. Efron and C. Stein, The Jackknife Estimate of Variance, The Annals of Statistics **9**, 586 (1981).
- [54] A. Sandvik, Stochastic method for analytic continuation of quantum monte carlo data, Phys. Rev. B **57**, 10287 (1998).
- [55] K. S. D. Beach, Identifying the maximum entropy method as a special limit of stochastic analytic continuation, eprint [arXiv:cond-mat/0403055](https://arxiv.org/abs/cond-mat/0403055) (2004), [cond-mat/0403055](https://arxiv.org/abs/cond-mat/0403055).
- [56] F. F. Assaad, Spin, charge, and single-particle spectral functions of the one-dimensional quarter filled holstein model, Phys. Rev. B **78**, 155124 (2008).
- [57] M. Ulybyshev, N. Kintscher, K. Kahl, and P. Buividovich, Schur complement solver for quantum monte-carlo simulations of strongly interacting fermions, Computer Physics Communications **236**, 118 (2019).
- [58] M. Hohenadler, F. Parisen Toldin, I. F. Herbut, and F. F. Assaad, Phase diagram of the kane-mele-coulomb model, Phys. Rev. B **90**, 085146 (2014).
- [59] M. Levin and T. Senthil, Deconfined quantum criticality and néel order via dimer disorder, Phys. Rev. B **70**, 220403 (2004).
- [60] T. Senthil, L. Balents, S. Sachdev, A. Vishwanath, and M. P. A. Fisher, Quantum criticality beyond the landauginzburg-wilson paradigm, Phys. Rev. B **70**, 144407 (2004).
- [61] T. Senthil, A. Vishwanath, L. Balents, S. Sachdev, and M. P. A. Fisher, Deconfined quantum critical points, Science **303**, 1490 (2004).
- [62] A. Tanaka and X. Hu, Many-body spin berry phases emerging from the  $\pi$ -flux state: Competition between antiferromagnetism and the valence-bond-solid state, Phys. Rev. Lett. **95**, 036402 (2005).
- [63] T. Senthil and M. P. A. Fisher, Competing orders, nonlinear sigma models, and topological terms in quantum magnets, Phys. Rev. B **74**, 064405 (2006).
- [64] Y. Liu, Z. Wang, T. Sato, M. Hohenadler, C. Wang, W. Guo, and F. F. Assaad, Superconductivity from the condensation of topological defects in a quantum spin-hall insulator, Nature Communications **10**, 2658 (2019).
- [65] X. Cai, Z.-X. Li, and H. Yao, Antiferromagnetism induced by electron-phonon-coupling, [arXiv:2102.05060](https://arxiv.org/abs/2102.05060) (2021), [arXiv:https://arxiv.org/abs/2102.05060](https://arxiv.org/abs/2102.05060) [cond-mat.str-el].
- [66] R. A. Jishi, *Feynman Diagram Techniques in Condensed Matter Physics* (Cambridge University Press, Cambridge, 2013).
- [67] R. Heid, The physics of correlated insulators, metals, and superconductors (Verlag des Forschungszentrum Jülich, Jülich, 2017) Chap. 15. Electron-Phonon Coupling, ISBN 978-3-95806-224-5.